

A Regional Model Study of Synoptic Features over West Africa

LEONARD M. DRUYAN AND MATTHEW FULAKEZA

Center for Climate Systems Research, Columbia University, NASA Goddard Institute for Space Studies, New York, New York

PATRICK LONERGAN

Science Systems and Applications, Inc., NASA Goddard Institute for Space Studies, New York, New York

MAHAMAN SALOUM

Direction de La Météorologie Nationale, Niamey, Niger

(Manuscript received 23 February 2000, in final form 8 November 2000)

ABSTRACT

Synoptic weather features over West Africa were studied in simulations by the regional simulation model (RM) at the NASA Goddard Institute for Space Studies. These pioneering simulations represent the beginning of an effort to adapt regional models for weather and climate prediction over West Africa. The RM uses a Cartesian grid with 50-km horizontal resolution and 15 vertical levels. An ensemble of four simulations was forced with lateral boundary conditions from ECMWF global analyses for the period 8–22 August 1988. The simulated midtropospheric circulation includes the skillful development and movement of several African wave disturbances. Wavelet analysis of midtropospheric winds detected a dominant periodicity of about 4 days and a secondary periodicity of 5–8 days. Spatial distributions of RM precipitation and precipitation time series were validated against daily rain gauge measurements and International Satellite Cloud Climatology Project satellite infrared cloud imagery. The time–space distribution of simulated precipitation was made more realistic by combining the ECMWF initial conditions with a 24-h spinup of the moisture field and also by damping high-frequency gravity waves by dynamic initialization. Model precipitation “forecasts” over the central Sahel were correlated with observations for about 3 days, but reinitializing with observed data on day 5 resulted in a dramatic improvement in the precipitation validation over the remaining 9 days. Results imply that information via the lateral boundary conditions is not always sufficient to minimize departures between simulated and actual precipitation patterns for more than several days. In addition, there was some evidence that the new initialization may increase the simulations’ sensitivity to the quality of lateral boundary conditions.

1. Introduction

The rainy season in West Africa is June–September and African wave disturbances (AWD) and squall lines are important precipitation triggers (Peters et al. 1989). Typical AWD wavelengths are about 2500 km (Burpee 1972), but convergence zones, vertical motion extremes, and squall lines are often confined to one wave sector (Reed et al. 1977). According to Kamara (1986), considerable precipitation also occurs within moist monsoon flows not associated with AWD. Recurring Sahel droughts with negative socioeconomic impacts reinforce the importance of improving our understanding of the interannual variability of this region’s climate. In addition, improved daily weather forecasts offer obvious benefits to many sectors of society.

The study of the local weather and climate of West Africa should appropriately relate to the analysis and simulation of AWD and their associated mesoscale structures. For diagnostic or predictive studies, the scale of perceived spatial details of these weather making systems depends on the horizontal resolution of the meteorological analysis/simulation model grid lattice. Druyan et al. (1997) showed that spatial features related to divergence and vertical motion near AWD became better defined when European Centre for Medium-Range Weather Forecasts (ECMWF) analysis resolution was increased from $4^{\circ} \times 5^{\circ}$ to $2^{\circ} \times 2.5^{\circ}$.

Reed et al. (1988) investigated the structure of AWD in the ECMWF operational analysis and forecast system’s gridded datasets for August–September 1985. Physical parameterizations in the ECMWF model used in the study had previously been revised and resolution had been increased to T106 (equivalent to 1.1° horizontal resolution). Patterns of 700-mb vorticity variance in the 3–5-day frequency band from these data identified

Corresponding author address: Dr. Leonard M. Druyan, Center for Climate Systems Research, Columbia University at NASA/GISS, 2880 Broadway, New York, NY 10025.
E-mail: LDruyan@giss.nasa.gov

AWD trajectories across West Africa along 12° and 22°N, but associated precipitation patterns were not studied. Semazzi et al. (1993) simulated the climate of West Africa for the summers of 1950 and 1984 with an 80-km horizontal resolution nested regional model. While their study examined mean precipitation fields, it did not consider the role of AWD. Jenkins (1997) discussed similar results at 110-km resolution for the contrasting 1988 and 1990 summers. Xue and Shukla (1993) used a high-resolution global model to demonstrate the negative impact of deforestation on AWD-related precipitation over West Africa during one season.

Druyan et al. (1996) related the precipitation recorded at Niamey (Niger) to the AWD of 10–11 August 1988, and Druyan et al. (1997) investigated its structure at 2° × 2.5° resolution. Neither study referred to the concurrent spatial distribution of precipitation over West Africa.

Sun et al. (1999a,b) described climate simulations made over eastern Africa at 60-km resolution using the Regional Climate Model version 2 (RegCM2) model of the National Center for Atmospheric Research. They found it prudent to customize the model by tuning it to the observed October climate (Sun et al. 1999a) before they applied it to the simulation of interannual variability. Sun et al. (1999b) discussed how ENSO and synoptic features of the large-scale circulation are related to simulated precipitation anomalies, but they did not discuss how the model's high horizontal resolution may have improved the analysis of near-surface circulation and temperature compared to the coarser gridded ECMWF data that were driving the model.

We have previously documented the performance of the National Aeronautics and Space Administration Goddard Institute for Space Studies (GISS) regional model (RM) during one 7-day period during August 1988. The RM exploits the considerably higher, 50-km resolution of a limited-area atmospheric model in order to better analyze the spatial structure of meteorological fields associated with synoptic features over West Africa. The model domain, 20°S–35°N, 35°W–35°E, includes the region of AWD formation in the eastern Sahel, the region of cross-equatorial flow in the Gulf of Guinea, the entire Sahara, and Atlantic coastal waters. Druyan et al. (2000) (hereafter DFT) showed reasonably skillful RM circulation forecasts at midtroposphere, but poor time-space distribution of simulated precipitation. A common evolution in those 16 simulations was excessive rainfall during the first two days, followed by almost no precipitation afterward. Subsequent testing found that the deficiency could be overcome by modifying the initial moisture field supplied from ECMWF analyses as discussed in section 3.

The current study describes new simulations of West African circulation and precipitation by the GISS RM, which uses an initialization procedure to improve results. Initial conditions, taken from ECMWF gridded

global analyses, are for 1200 UTC 8 August 1988 and the simulations continue to the end of 22 August 1988. An ensemble of four RM atmospheric simulations over West Africa are considered along with five additional simulations designed to evaluate the time rate of forecast deterioration and the relative importance of lateral boundary conditions. The uniqueness of these efforts is the application of a relatively high-resolution regional model to problems of weather prediction in this area. While this investigation focuses on model performance for selected case studies of the evolution of daily circulation and precipitation over West Africa, future work will consider seasonal climate means and multiyear validation statistics. In all, 10 simulations covering all or part of a 2-week period in August 1988 are considered here.

2. Regional model

The regional model (RM) at GISS was derived from a version developed at The Florida State University (FSU). The RM has the same basic structure as the FSU global spectral model (Ross 1991), except it uses a Cartesian grid with 50-km spacing for dynamics and incorporates special treatment of soil moisture especially developed by Fulakeza (1998) for studies over Africa. Early versions were used by Kumar (1989) and Krishnamurti et al. (1990), the latter in a study demonstrating the positive impact of horizontal resolution on tropical predictions. The current version of the RM was described by DFT. The RM solves the primitive equations on 15 sigma surfaces using a semi-Lagrangian advection scheme and semi-implicit time differencing. The treatment of long- and shortwave radiation transfer includes diurnal and seasonal variations, absorption by greenhouse gases, and interactive clouds. Terrain topography is specified at 50-km resolution, consistent with the horizontal computing grid.

Deep convection is parameterized by the Kuo (1974) scheme, but it has been modified according to Krishnamurti et al. (1983, 1990). According to the original formulation, moistening and heating by the convective cloud are proportional to the humidity and temperature differences between the cloud and its environment. The proportion of the available heat and moisture supply that is assumed to be added to the column by cumulus convection must be assigned. To improve the match between simulated and observed rainfall, Krishnamurti et al. (1983, 1990) introduced mesoscale moisture convergence and moistening parameters. The mesoscale convergence is regarded as nonmeasurable and subgrid scale.

In the modified scheme, the parameterization determines the moisture convergence and moistening parameters from knowledge of large-scale variables. Krishnamurti et al. (1983, 1990) showed that the large-scale vertically integrated vertical velocity and lower-troposphere (700 mb) relative vorticity can serve as suc-

cessful proxies for the mesoscale moisture convergence and moistening parameters in the modified Kuo scheme. In the RM, the parameterization of cumulus convection follows this modified Kuo scheme. Deep cumulus convection is invoked when the atmosphere is conditionally unstable, vertical motion is upward, and a net supply of moisture convergence is available. To improve computing efficiency, the cloud base is taken to be at the lowest model level at which the relative humidity is greater than 0.8 while satisfying the above conditions (instead of determining the cloud base through a lifting condensation procedure). The thermodynamic structure within the cloud is obtained by constructing a moist adiabat from the cloud base. It is assumed that the moist static energy is conserved along this moist adiabat. The cloud top is defined as the level at which the cloud temperature is less than the temperature of the environment.

The basis of the present soil moisture parameterization was developed by Dastoor and Krishnamurti (1991) and improved by Bounoua (1992) and more recently by Fulakeza (1998). Soil moisture availability (SMA) is defined as the ratio of soil moisture at the surface to a maximum saturation value (field capacity). Second-order regression equations for SMA were developed as functions of observed 5-day rainfall, albedo, surface temperature, normalized difference vegetation index (NDVI), and terrain relief, in order to account for the response of both the soil morphology and the climate forcing. The computation of preliminary SMA for the regression analysis was based on estimates of evaporation (latent heat flux) derived from moisture continuity considerations and computation of the surface radiative energy balance (see Dastoor and Krishnamurti 1991). The derived regression equations (one for each of three soil types) are used by the RM to predict SMA during model simulations. NDVI is updated biweekly from satellite radiometric observations while land surface albedo evolves during the simulation according to variations in SMA, following Deardoff (1978). Accordingly, SMA is computed interactively as a function of model rainfall, albedo, and surface temperature, as well as observed NDVI. Fulakeza (1998) showed that RM-predicted soil moisture and albedo have an impact on simulated rainfall over southern Africa through the modification of sensible and latent heat fluxes. The current study does not attempt to evaluate the impact of the SMA scheme on the simulations. Accordingly, it does not address the potentially important influence that SMA variability may have on the daily circulation or on precipitation rates over West Africa.

Prescribed lateral boundary conditions (LBC) are merged with the predicted RM evolution by weighting them with progressively decreasing weights inward within a buffer zone that completely surrounds the domain of interest. Accordingly, model-computed fields along the lateral boundaries are smoothed to prevent high gradients between the driving analysis (outside)

and model-computed variables within the domain. Optimal treatment of this approach avoids overdamping of incoming waves, but care must also be taken not to create reflections by too sharp a transition. The buffer zone consists of n grid elements and the relative weights (wt) of the LBC vary according to the formulation,

$$\text{wt} = k \exp(-p r), \quad (1)$$

where k and p are coefficients that determine the relative influence of the LBC and r is the row number from 1 to n . For the present simulations, the best results were obtained by using a buffer zone consisting of six grid elements ($n = 6$), $k = 2.2$, and $p = 0.8$.

3. Initialization and experiments

A more realistic time-space distribution of precipitation, as compared to the results of DFT, is consistently obtained by modifying the initial moisture and circulation fields to improve their compatibility with the RM. After testing several approaches, we settled on a procedure for preprocessing ECMWF three-dimensional moisture distributions that gives encouraging results.

The humidity initialization procedure uses 24-h “predicted” relative humidities valid at t_0 (the beginning of the model simulation). The prediction is made in a preprocessing simulation that begins with ECMWF data at $t_0 - 24$ h. The resulting “spinup” values of relative humidity are then combined with ECMWF temperatures at t_0 to compute the initial specific humidity [$Q(t_0)$] at all levels. For the experiments described here, the preprocessing simulation began with ECMWF data at 1200 UTC 7 August 1988. Relative humidity values predicted after 24 h (at t_0) by this spinup simulation, together with ECMWF temperatures for 1200 UTC 8 August, then formed the basis for recomputing $Q(t_0)$. The resulting $Q(t_0)$ replaced Q in the ECMWF dataset for 1200 UTC 8 August.

Overall results are additionally improved by “dynamic initialization,” a procedure that eliminates high-frequency gravity waves from the circulation fields given by ECMWF datasets. This step somewhat modifies surface pressures, geopotential heights, and temperatures, but retains the same specific moisture distribution that is computed during the spinup cycle.

We employed the dynamic initialization described in detail by Krishnamurti et al. (1990) and based on the dynamic normal-mode initialization proposed by Sugi (1986). This method utilizes a forward-backward iteration of the linear terms around the first time step while keeping the nonlinear forcings fixed. After every 100 linear iterations the nonlinear terms are updated and the entire cycle is repeated. Efficient application of the procedure damps high-frequency gravity waves faster than meteorologically significant lower-frequency waves. Based on this criteria, the time integration scheme for the forward-backward iterations that was chosen by Krishnamurti et al. (1990), and used with the prede-

cessor of the GISS RM, was a Eulerian scheme previously suggested by Okamura (see Haltiner and Williams 1980).

Model surface boundary conditions also include observed NDVI over land and observed sea surface temperatures over ocean grid elements.

Giorgi and Mearns (1999) recommend that an RM first be evaluated using observational analyses for LBC. ECMWF analyses over sparse data regions such as West Africa provide somewhat less than “perfect LBC,” but they are anchored to the observed meteorology. In the experiments described below, ECMWF data from gridded analyses convey information to the regional model in order to represent the influence of large-scale circulation and global forcings. A thorough evaluation of RM skill based on observed LBC contributes to the interpretation of future downscaled GCM results.

The simulations described below were forced with LBC that were time and space interpolated from ECMWF analyses every 12 h. Random perturbations of $-1.5 \text{ mb} < P < +1.5 \text{ mb}$ were applied to the initial surface pressure field in order to create four arbitrarily different sets of initial conditions. The ensuing four simulations were combined to form an ensemble average, referred to below as ENS. However, the study also includes several experiments that were based on single simulations.

4. Precipitation validation

a. Spatial distributions of ENS daily precipitation

9 August: Figure 1a shows the streamflow pattern at 700 mb from ECMWF $2.5^\circ \times 2.5^\circ$ resolution analyses (hereafter EC) based on zonal and meridional wind components averaged for 0000 and 1200 UTC on 9 August 1988. The most prominent AWD trough over West Africa is in the vicinity of Lake Chad near 12°E (hereafter AWD1). An additional wave (AWD2) is analyzed near 3°W and a sharp trough appears along 10°N (hereafter the Gulf Coast Trough, GCT). The simulated circulation (Fig. 1b), based on zonal and meridional wind components averaged over eight synoptic times at 3-h intervals, 0000–2100 UTC, represents AWD1, AWD2, and the GCT quite well.

One of the problems encountered in the original set of simulations (DFT) was excessive rainfall during the first day. The initialization procedure succeeded in reducing rainfall amounts on day 1 of the simulation (Fig. 1b) and in confining the more realistic precipitation maximum (about 10 mm) to a smaller area that corresponds quite well to the observed distribution and to satellite imagery (Figs. 1c, 1d).

10 August: Inspection of the EC 700-mb streamflow analysis for 10 August 1988 (Fig. 1e) reveals only a small westward advance of the northern end of the AWD1 trough during the last 24 h. In addition, a well-formed AWD2 remains near 3°W and the breakdown of

the GCT is noted. National Centers for Environmental Prediction (NCEP) reanalyses confirm the longitude of AWD1 along 12°E on 10 August (not shown), but with a less pronounced westward tilt. In addition, NCEP reanalyses show a much shallower AWD2 at 5°W . AWD2 is still evident in the model’s circulation field (Fig. 1f), which also features a realistic tilt for AWD1.

The modeled precipitation areas (Fig. 1f) are situated close to and downstream from the AWD1 trough. The corresponding satellite image (Fig. 1g) shows a shield of bright clouds along about 6°E , some 4° ahead of the trough. Station reports (Fig. 1h) indicate precipitation over a 12° swath westward from the trough line with heaviest amounts between 0° and 5°E . Overall, the spatial distribution and the amounts of simulated precipitation are quite realistic.

11 August: The EC 700-mb circulation (Fig. 1i) has reorganized into a large amplitude wave that dominates much of West Africa. There is evidence (not shown) that AWD1 and AWD2 merged before noon on the 11th. We continue to refer to this system as AWD1, which is linked to a closed cyclonic vortex over southern Nigeria on 11 August. The EC analyses indicate that the AWD1 trough advanced some 5° longitude between 0000 UTC (7.5°E) and 1200 UTC (2.5°E) on 11 August, and NCEP reanalyses indicate a similarly timed reorganization of AWD1. The modeled circulation correctly depicts the broader AWD1 trough with a realistic tilt.

The center of the modeled precipitation area (Fig. 1j) has moved westward of its previous position and it is not far from where the satellite image (Fig. 1k) positions a convective complex and where station observations (Fig. 1l) validate the more than 20 mm in simulated rainfall. Simulated and observed precipitation fields overlap, but the maxima are displaced relative to one another by several degrees. The broadest precipitation area remains downstream of the AWD1 trough, although both simulated and observed fields indicate a small area of heavy rainfall along 10°E where the broad trough maintains some cyclonic vorticity.

12 August: The simulated circulation pattern (Fig. 1n) resembles the EC analysis (Fig. 1m); AWD1 has moved to the vicinity of 2°E and is associated with a cyclonic vortex at 0° . A much reduced area of rainfall at 10°W continues the model’s pattern of precipitation downstream of the AWD1 trough, but it corresponds to only shallow clouds (Fig. 1o) and no measured precipitation (Fig. 1p), although some rain is reported farther downstream near the edge of bright clouds along the Atlantic ITCZ. The single observation of 33 mm at Fada N’Gourma (12°N , 0° , Burkina Faso) is suspiciously high in an area where no clouds are evident. On the other hand, the observation of 33 mm at Tessalit (20°N , 1°E , Mali) (not simulated) does correspond to a bright cloud cluster. Satellite and station data agree that the broadest area of convective activity occurs between 3° and 15°E , within southeasterly circulation. The model shows only an isolated area at 11°E (Fig. 1n). This fourth day of

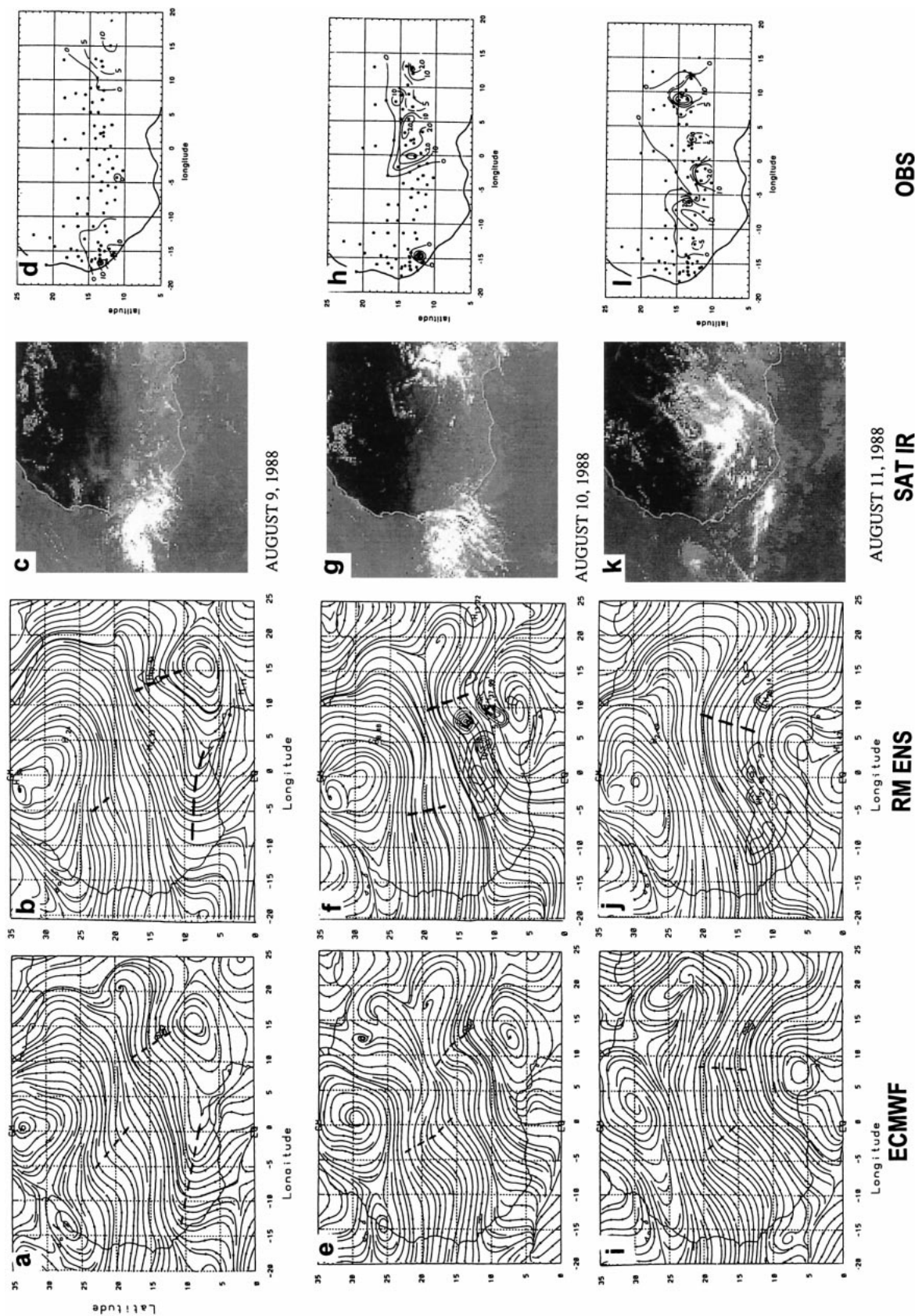


FIG. 1. (a)–(z') Circulation at 700 mb, 24-h precipitation totals and cloud imagery for each day, 9–15 Aug 1988. (left) ECMWF 0000 UTC and 1200 UTC resultant winds. Dashed lines indicate major troughs. (second from left) ENS resultant winds of 3-h hourly fields. ENS precipitation contours are given at 5-mm intervals. (second from right) ISCCP B3 infrared imagery at 1500 UTC. (right) Spatial distribution of observed precipitation (mm) based on rain gauge measurements (whose locations are indicated by dots).

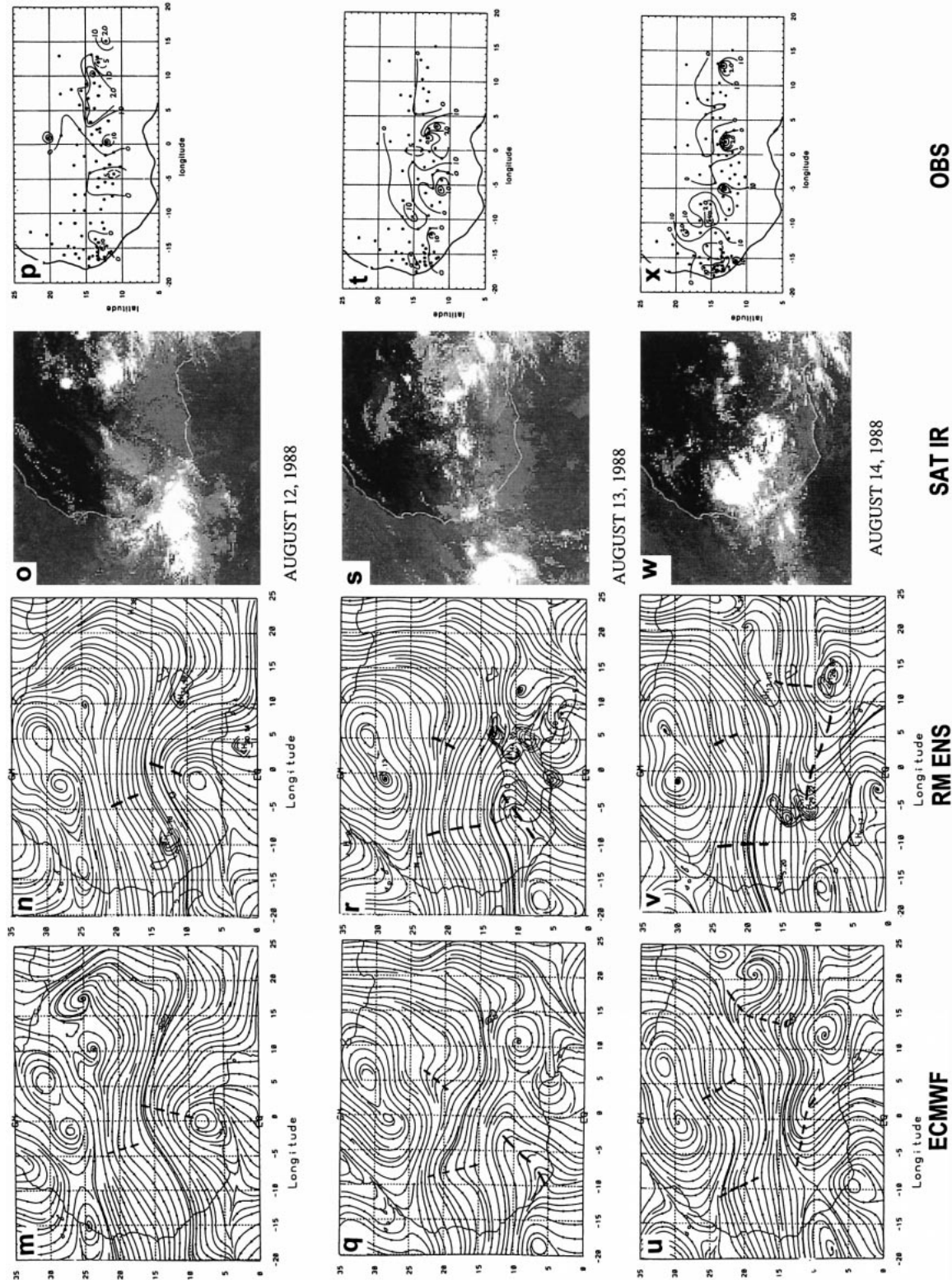


FIG. 1. (Continued)

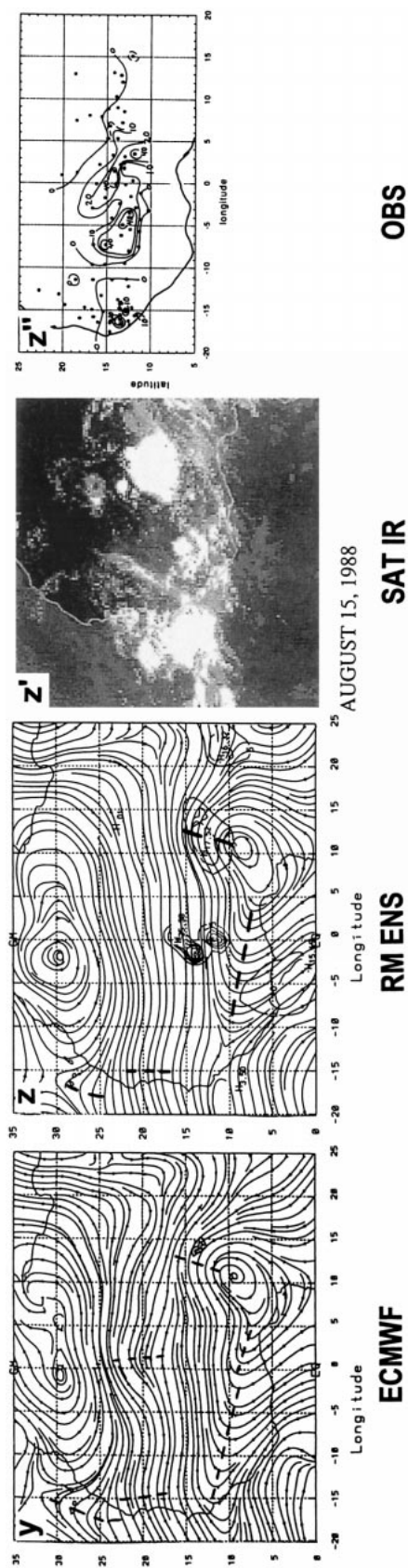


FIG. 1. (Continued)

the sequence evidences a marked deterioration between simulated and observed precipitation distributions.

13 August: The circulation simulation correctly generates a new cyclonic center south of Lake Chad (Fig. 1r compared to Fig. 1q) and includes other realistic features, such as AWD1 reaching 8°W. Widespread precipitation (Fig. 1t), slightly underestimated by the simulation (Fig. 1r), is associated with the northeast pointing trough near 5°W and also with convergence downstream from the new cyclonic center near 4°E. Satellite imagery (Fig. 1s) shows a northwest–southeast squall line approximately corresponding to the rather heavy rates of modeled precipitation near 3°–5°E. Simulated precipitation amounts between 0° and 5°E reach about 44 mm (Fig. 1r) and correspond to observations ranging between 10 and 50 mm (Fig. 1t). However, the model fails to generate any precipitation west of 6°W where a number of stations report light rainfalls.

14 August: NCEP and EC (Fig. 1u) analyses agree on the appearance of a wave in the northeasterlies at about 4°E on 14 August (hereafter AWD3), and this wave appears in the day 6 model prediction (Fig. 1v). In addition, NCEP and EC show the reorganization of a northwest–southeast-oriented GCT (AWD4) along 12°N and the simulation remarkably follows the same sequence. In addition, a new wave forming near Lake Chad (AWD5) on 14 August is also indicated by the modeled circulation. The northwest-to-southeast line of convective rainfall has intensified (Fig. 1x) contributing to accumulations in excess of 20 mm at many stations. The corresponding satellite image (Fig. 1w) shows that by 1500 UTC the convective complex is closer to the Atlantic coast than the 24-h precipitation observations would indicate. The simulation greatly underestimates the spatial extent of this convective complex whose dynamic trigger is unclear from the analyzed or simulated circulation. In effect, the model reproduces only the southeastern end (5°W), indicating reasonable rates in excess of 20 mm. There is also evidence of isolated pockets of precipitation between 0° and 10°E where the model is showing no rainfall (Fig. 1v), and at 12°E, which was simulated with a small southward displacement.

15 August: The positions and configurations of the troughs appearing in the corresponding EC analysis (Fig. 1y) are all well represented in the circulation simulation shown in Fig. 1z, except that AWD3 has perhaps been damped too much.

Station data and satellite imagery (Figs. 1z', z'') refer to a large convective complex spanning about 10° longitude and centered near 0°. One possible trigger is the GCT, but we also note that AWD5 is some 10° upstream from this activity. The model has indeed suggested a limited area of moderate rainfall at this location (Fig. 1z). While the simulated precipitation rates of up to 35 mm are reasonable, the area covered by the rainfall is considerably underestimated. In addition, rather bright satellite cloud images corresponding to the offshore ITCZ are also not matched by the model. Modeled rain-

fall along the AWD5 trough corresponds to several observations of very light accumulations.

We compared the 700-mb circulation of these experiments with the results of DFT and found that the improvements in the time-space distribution of precipitation had a slight positive impact on the simulated circulation. For example, the formation of a northeast-southwest-oriented trough over the southwest coastal area (Ivory Coast) on 13 August was handled better by these simulations. Also, on 15 August, the circulation over most of the domain is correctly more zonal than in the results of DFT and the newly developed AWD near Lake Chad better resembles the EC validation than in DFT. We postulate that the more realistic distribution of latent heat sources improved the simulation of horizontal temperature gradients, hence circulation.

b. Precipitation time trends

We validated the time trend of modeled ENS daily precipitation against station data over three areas. The first area average, comprising only four grid points, was compared to collocated observations from three stations (Fig. 2a); the second area average of 12 grid points was compared to six stations (Fig. 2b), and the third area of 162 grid points was compared to 18–19 stations (Fig. 2c). The results show that the correspondence between modeled precipitation and observations is reasonable at all three spatial scales for the first 2 days. Increasing the size of the target area from 4 to 12 grid points improves the match on day 3. Increasing the target area to 162 grid points improves the match also for days 4–5. The discrepancy on 15 August is because the observed maximum was not simulated over a wide enough area. The results reflect model limitations in locating the exact position of rainfall maxima on a particular day. Since increasing the target area forgives spatial displacement errors, the correspondence improves for the larger areas. Beyond the favorable results for the initial days, RM precipitation time series for these areas are not correlated with observations. This implies that information contained in the initial conditions was important for simulating rainfall. Although updated LBC convey something of the actual meteorological evolution to the region during the entire simulation, these data are apparently insufficient to force accurate evolution of the precipitation field. We tested whether reinitializing with EC data improves the modeled precipitation field. A single new run was begun from the EC dataset of 1200 UTC on 13 August 1988; moisture and dynamic initialization were applied, as before. The resulting improvement in precipitation rates over the three validation areas can be seen in Fig. 2. In each case precipitation rates on both the first and second full days (14–15 August) were much higher than for ENS. Moreover, in this reinitialized simulation, the maxima of 14–15 August were correctly followed first by decreases and then by a small increase on 21 August, closely

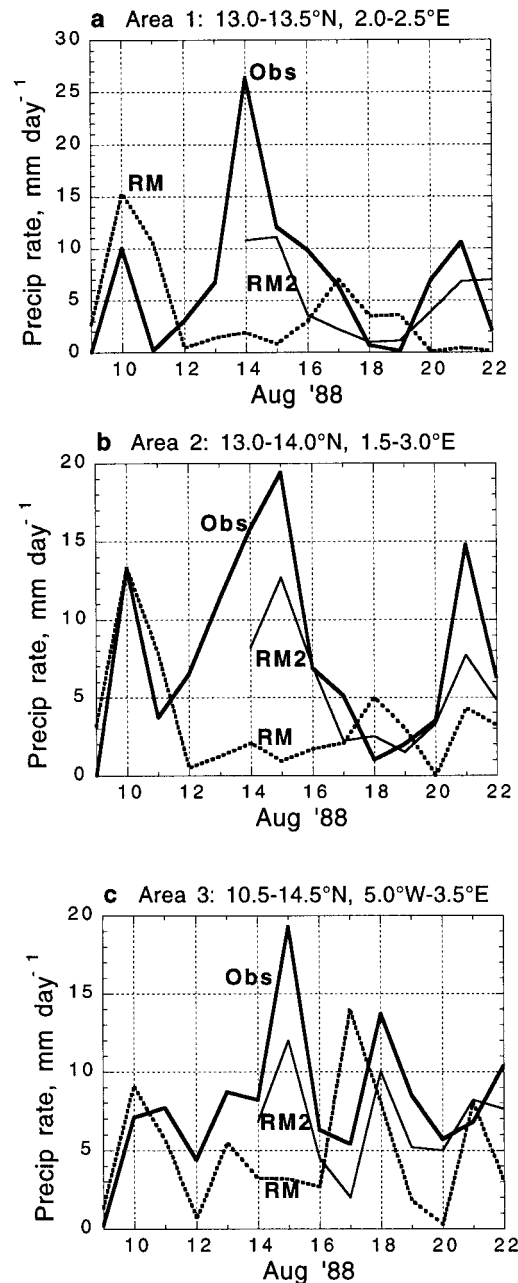


FIG. 2. Validation of area-averaged daily precipitation totals. (a) "Obs" refers to the mean of three rain gauges within the designated area. "RM" refers to ENS results representing the mean of the four grid points bordering the designated area. "RM2" is like "RM" but for the single simulation initialized at 1200 UTC 13 Aug 1988. (b) Same as (a), except "Obs" refers to the mean of six rain gauges within the designated area and "RM" refers to ENS results representing the mean of the 12 grid points bordering the designated area. (c) Same as (a), except "Obs" refers to the mean of 18–19 rain gauges within the designated area and "RM" refers to ENS results representing the mean of the 162 grid points bordering the designated area.

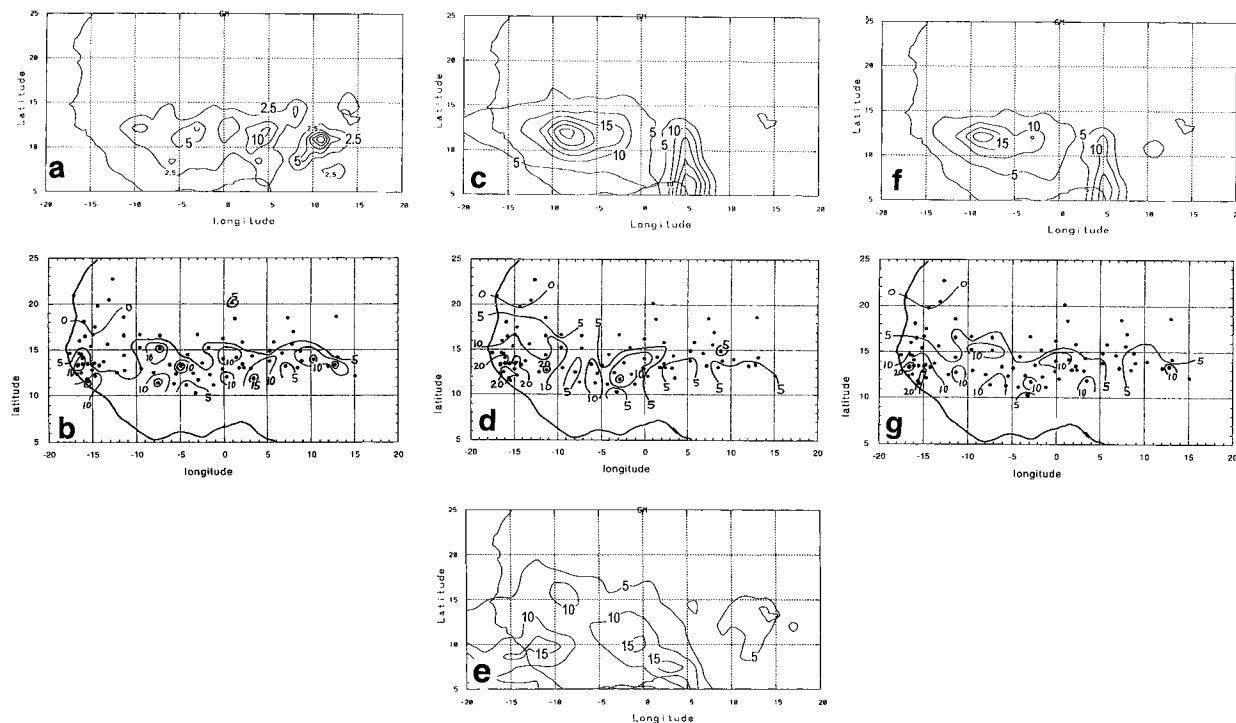


FIG. 3. Spatial distributions of time-averaged precipitation rates (mm day^{-1}). ENS results for (a) 9–15 Aug 1988, (c) 16–22 Aug 1988, and (f) 9–22 Aug 1988. Observed distributions based on rain gauge measurements (station locations indicated) for (b) 9–15 Aug 1988, (d) 16–22 Aug 1988, and (g) 9–22 Aug 1988. (e) RM results for 16–22 Aug 1988 based on a single simulation initialized at 1200 UTC 13 Aug.

paralleling the observational trend. The skill of this precipitation simulation perseveres some 8–9 days, considerably longer than for ENS. Additional testing is needed to determine whether the duration of skillful precipitation simulations is generally so variable. We suspect that such variability may be related to the quality of the initial state data and/or the complexity of the evolving meteorology.

c. Weekly mean precipitation distributions

The spatial distribution of mean modeled ENS precipitation rates for 9–15 August (Fig. 3a) shows a swath over West Africa that is nearly symmetric about 12°N , with several maxima reaching between 6 and 15 mm day^{-1} . According to station observations (Fig. 3b), the latitude interval between 10° and 15°N during the period 9–15 August 1988 experienced total accumulations mostly between 5 and 15 mm day^{-1} . Modeled amounts were generally lower than the observed values, but the model correctly simulated the broadest swath of precipitation east of 10°W . Heavy rainfall observed along the Atlantic coast was not simulated. The time series for the central Sahel (Fig. 2) shows that much of the model's rainfall deficit occurred on 14–15 August. For 15 August the model has managed only a small fraction of the observed rainfall. Figure 3d shows that during the second week, precipitation accumulations exceeding 10 mm are confined to the west of 0° longitude, with

the highest values near the Atlantic coast. The simulation (Fig. 3c) has produced realistic rates that reflect a westward shift into the second week, although the modeled maximum is displaced about 7° eastward of the observed location. The simulated spatial distribution of second-week precipitation by the single run that was initialized on 13 August (1200 UTC), which appears as Fig. 3e, shows excellent agreement with the observed distribution, although the Atlantic coast maximum should have extended to higher latitudes. The ENS 2-week mean distribution (Fig. 3f) shows a larger area of rates exceeding 10 mm day^{-1} than can be interpreted from rain gauge measurements (Fig. 3g) and the simulated precipitation is conspicuously deficient along the Atlantic coast.

5. Vorticity at 700 mb

DFT showed how AWD are conveniently tracked on time-longitude cross sections of vorticity due to the zonal gradient of the meridional wind at 700 mb ($\zeta \equiv \Delta v / \Delta x$). The time-longitude cross section for ENS ζ , based on 3-h resolution, is shown in Fig. 4a and can be compared to the same diagnostic for EC in Fig. 4b (based on 12-h resolution). The ENS AWD1 appears as a diagonal ribbon of maximum ζ that begins on 8 August near 15°E and can be traced to about 25°W on 15 August, implying a speed of about 7 m s^{-1} . The modeled AWD1 follows the same path as the EC analyzed

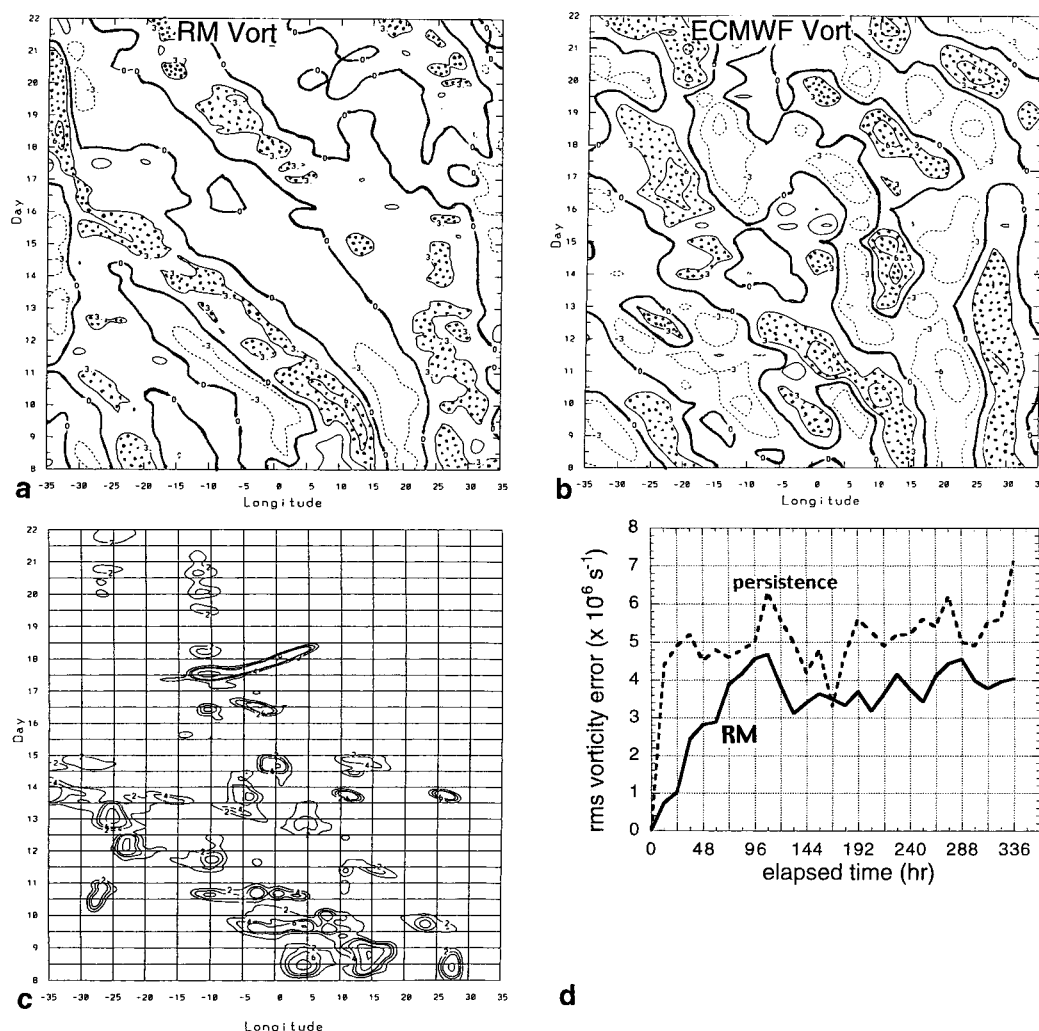


FIG. 4. Time-longitude distribution of 700-mb vorticity due to the zonal gradient of the meridional wind ($\zeta \equiv \Delta v / \Delta x$) averaged over 12° – 20°N . (a) RM ENS at 3-h intervals, (b) ECMWF at 12-h intervals. Here $\zeta = 0$ is bold and ζ maxima are stippled. (c) Time-longitude distribution of ENS precipitation rate averaged over 10° – 20°N . Contours are 2, 4, 6, 8, 10 mm day^{-1} . (d) Root-mean-square of ENS errors in ζ at 12-h intervals, validated against ECMWF analyses within the area 5° – 25°N , 25°W – 15°E . Persistence errors represent the rms ζ differences between the ECMWF analysis at 1200 UTC 8 Aug 1988 and subsequent ECMWF ζ fields. Units for ζ : 10^{-6} s^{-1} . Labels along vertical axes in panels a–c indicate 1200 UTC on the designated day.

AWD1, until it moves out over the Atlantic where the EC analysis is given fewer observations. Elsewhere on these charts, there are both agreements and disagreements between ENS and EC regarding other ζ maxima. The RM results show better time continuity and therefore give smoother patterns.

Figure 4c shows the time-longitude distribution of simulated ENS precipitation. The diagonal progression of precipitation maxima across the chart indicates westward propagation of areas of active moist convection. Comparison with Fig. 4a shows that the eastern portion of one rain shield was situated within the quasi-stationary AWD1 ζ maximum during 8–9 August, but after AWD1 began to advance westward, the eastern edge was repositioned some 5° longitude downstream of the

ζ maximum. The next diagonal band of precipitation (passing through 5°E on 13 August) appears to move through negative vorticity and eventually reach the eastern edge of the AWD1 trough by 14 August. Reference to Fig. 1 fails to identify any single propagating synoptic feature that explains this rainband, except that other studies have found that the region immediately east of an AWD trough is often favored for precipitation because of enhanced moisture convergence within southeasterly circulation (Druyan et al. 1996).

The congruence of the simulated ζ spatial pattern with the corresponding EC ζ distribution is a measure of forecast skill that is sensitive to the handling of AWD, although EC analysis data represent an imperfect validation standard. Figure 4d shows the time trend of the

rms differences between ENS and EC spatial distributions of ζ at 12-h intervals over the part of the domain that is relevant to AWD (5° – 25° N, 15° E– 25° W). Rms ζ errors of persistence, also shown in Fig. 4d, are based on using the initial EC analysis as the forecast at each subsequent time step. The rms ζ error of persistence is already large after 12 h and it reaches $5 \times 10^{-6} \text{ s}^{-1}$ by the end of the first day. The rms ζ error for ENS, however, increases much more gradually during the first 108 h (4.5 days). It stabilizes at about $3.5 \times 10^{-6} \text{ s}^{-1}$ soon thereafter, and it increases only slightly during the second week. The rms ζ errors of the simulation ensemble are lower than persistence errors for the entire 2 weeks (except for the validation at 168 h). These results imply that the simulations of 700-mb circulation are quite skillful during the first 3–4 days while they retain some skill for indefinite durations.

6. Divergence

Divergence is the mechanism that links synoptic circulations with broadscale precipitation areas. The AWD composite constructed by Reed et al. (1977) included 850-mb convergence west of the trough and 200-mb divergence southwest of the apex, with maximum precipitation rates approximately where these centers overlap. The combination of lower-tropospheric convergence and upper-tropospheric divergence creates rising motions conducive to precipitation. Ideally, the AWD is sandwiched between anticyclonic ridges and descending branches associated with divergence below and convergence aloft, so that the complete circulation describes closed cells in the zonal plane. This conceptual structure is reflected in the modeled circulation on 11 August when the AWD1 700-mb trough was along 7.5° E. Figure 5a shows very strong 200-mb divergence centered on 0° and bracketed by convergence zones at 12.5° W and 17.5° E. The rising branch of the AWD1 circulation in the zonal plane is further indicated in Fig. 5b by 850-mb convergence centered on 0° , with divergence to the west (10° N, 12.5° W) and to the east (13° N, 15° E). Substantial precipitation, observed and modeled, is apparent within a 10° band under the rising node (Fig. 11), but a second area of precipitation at 10° E cannot be explained by the AWD circulation.

In this example, the divergence centers at 200 mb are much broader than at 850 mb, especially in the meridional direction. Horizontal displacements between the divergence maxima and corresponding minima at the two vertical levels imply vertical tilts of the rising and descending branches, such as have been previously discussed in the literature (Reed et al. 1988; Druyan et al. 1997).

One manifestation of the subsequent weakening of AWD1 is that the 200-mb divergence maximum all but vanished by 12 August (not shown). A new strong maximum reappears near the Atlantic coast on 14 August (not shown), corresponding to increases in observed

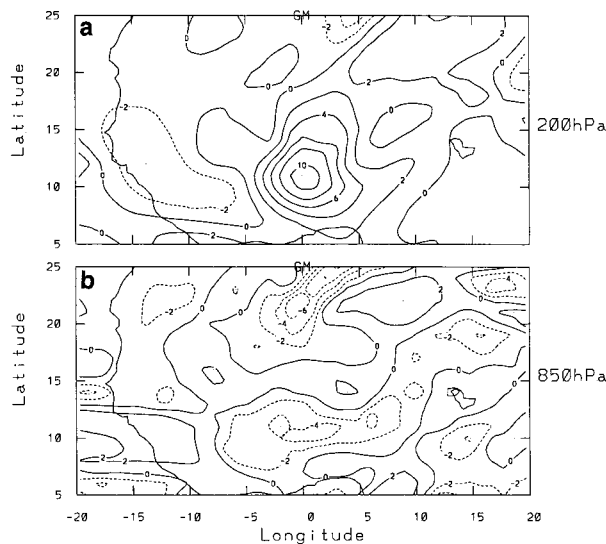


FIG. 5. Horizontal distributions of divergence computed for ENS resultant winds at (a) 200 mb and (b) 850 mb for 11 Aug 1988. Units: 10^{-6} s^{-1} .

precipitation there (Fig. 1x), which were not simulated (Fig. 1v). The major line of moist convective activity on that date was farther east near 5° – 10° W, but only some of that activity overlaps the uplift implied by divergence distributions.

Figure 6 shows that a swath of ENS 850-mb convergence propagated in tandem with AWD1, coinciding with the simulated precipitation (Fig. 4c) that preceded AWD1 (see Fig. 4a) across West Africa. The corresponding time-longitude distribution of 850-mb divergence based on EC analyzed winds (not shown) does not show this swath, presumably because of its coarser space-time resolution.

There is no consistent convergence pattern in Fig. 6 corresponding to the next swath of propagating precipitation (Fig. 4c), just as there was no vorticity maximum. Spatial distributions of 850-mb divergence show a strong north-to-south-directed gradient near 13° N over the central Sahel on 13–15 August, but the simulated precipitation is mostly within (850 mb) divergence. Plumes of uplift are often tilted (Reed et al. 1988; Druyan et al. 1997), and strong convergence was indeed present at 700–500 mb over these precipitation regions, implying that moist convection was probably initiated in the midtroposphere.

7. Periodicity

Spectral analysis is a more objective method for determining the periodicity of model-simulated AWD. However, much longer time series than those studied here are required to analyze spectral peaks relevant to AWD, namely, those with 3–9-day periods. Alternatively, wavelet analysis (Torrence and Compo 1998) offers the opportunity to detect the temporal variation of

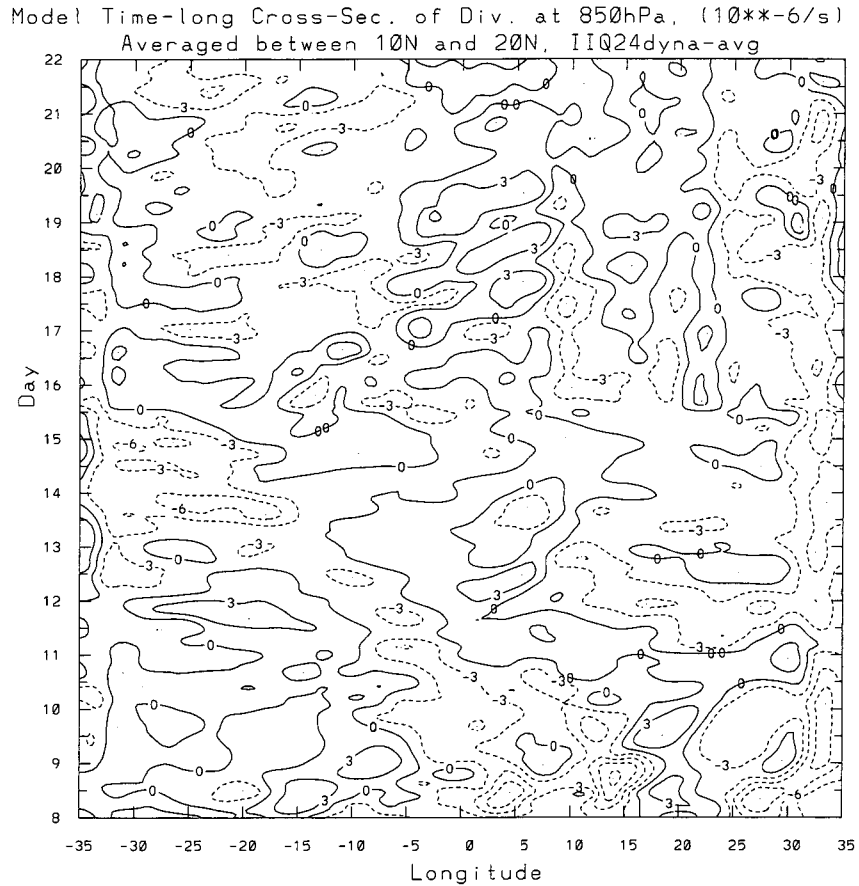


FIG. 6. Time-longitude distribution of ENS 850-mb divergence (10^{-6} s^{-1}) averaged over 10° – 20° N. Units: 10^{-6} s^{-1} .

spectral properties, even for short records. Diedhiou et al. (1999) applied wavelet analysis to the mean daily 700-mb meridional wind over West Africa from NCEP and ECMWF datasets for June–September 1988.

Figure 7 shows the wavelet results for the RM 700-mb meridional wind (v7) component at five locations over the model domain. Since the time series are relatively short compared with the dominant periodicities, spectral

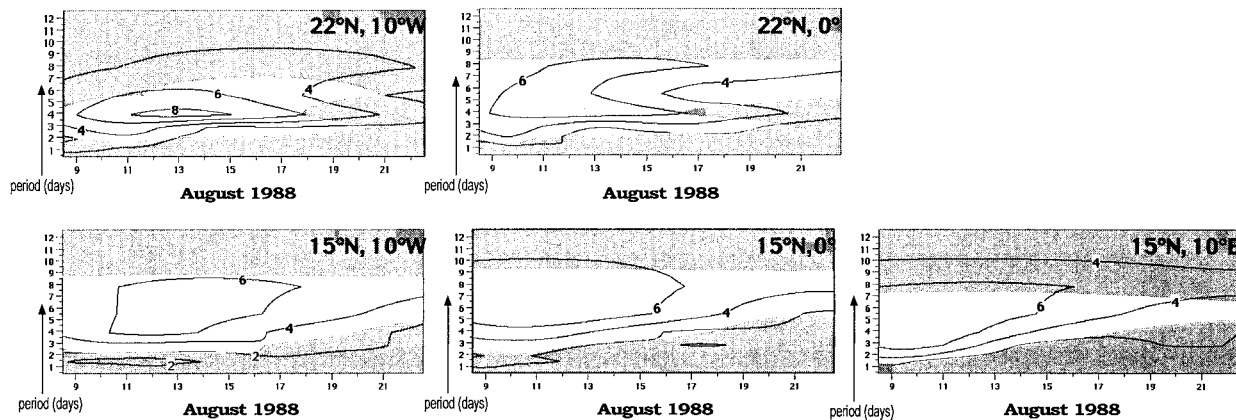


FIG. 7. Wavelet analysis of 700-mb meridional wind time series at five locations (coordinates given). Spectral amplitudes (m s^{-1}) have been averaged over the four simulations of ENS and are mapped against periodicity (vertical axis) and elapsed time (horizontal axis). Nonshaded areas indicate $>95\%$ probability that departures of the wavelet amplitude from a comparable red noise spectrum are statistically significant using a χ^2 distribution.

resolution is somewhat coarse. Within the range of interest, spectral amplitudes are computed for periods of 1.9, 2.8, 3.9, 5.5, and 7.8 days. The nonshaded areas in Fig. 7 indicate where there is greater than 95% probability that departures of the wavelet amplitude from a comparable red noise spectrum are statistically significant using a χ^2 distribution. The most frequent spectral maximum that was analyzed from this simulation was at 3.9 days (at three of the five grid points). This is consistent with many studies that found spectral peaks for AWD at periods between 3 and 5 days (Burpee 1972; Diedhiou et al. 1999). Figure 7 shows that at 15°N, 0° and 15°N, 10°W, 5–8-day periods dominate. The wavelet analysis for 15°N, 10°E also shows that the wave activity in the east was most prominent during the first week, while at 0° and 10°W, periodic variability of v7 was stronger into the second week.

8. Constant LBC

DFT had reported on a low sensitivity of RM simulations to constant LBC. This was a rather surprising result that was either a peculiarity of West African weather or those particular simulations. In order to address this matter, we repeated the 8–15 August simulation, but imposed constant LBC in two runs from arbitrarily varied initial conditions. (Random perturbations of $-1.5 \text{ mb} < P < +1.5 \text{ mb}$ were applied to the initial surface pressure field in order to create the second set of initial conditions.) Both constant LBC simulations severely damped amplitudes of simulated AWD and both caused a degradation of the ζ simulation, resulting in 25%–30% higher rms ζ errors compared with ENS after the fifth day. Moreover, these simulations underestimated rainfall over the central Sahel, and were accordingly less realistic than ENS. Damped AWD amplitudes may in part be explained by the fact that constant LBC do not allow periodic variations to enter via the lateral boundaries. Other explanations were sought by evaluating the following experiments.

Since the experiments described by DFT did not include the preliminary spinup of moisture or dynamic initialization, we tested their impact combined with constant LBC in two additional experiments. In one constant LBC run, all latent heat releases were eliminated in order to evaluate the role of latent heat feedbacks on the circulation. This simulation achieved somewhat more realistic midtropospheric circulation patterns than the two fully initialized constant LBC experiments, decreasing the rms ζ error by about 8%. The second constant LBC simulation, which used spinup moisture but not dynamic initialization, also improved the subsequent evolution of the midtropospheric circulation (15% decrease in rms ζ error). These results imply that the initialization process increases the RM sensitivity to the quality of LBC, but the effect cannot be demonstrated with objective statistical significance since conclusions are based on single simulations.

9. Conclusions

The RM simulations of West Africa summertime weather and climate at 50-km horizontal resolution offer unique opportunities to study the relationships between circulation and precipitation. The current simulations represent an improvement over previous RM results discussed in DFT. Better temporal and spatial distributions of simulated precipitation were achieved by introducing an initialization procedure that makes observed initial conditions more compatible with model physics. The procedure incorporates a 24-h spinup moisture field and an iterative dynamic forward-backward integration of the equations of motion in order to eliminate high-frequency gravity waves.

The RM simulations forced by synchronously updated ECMWF data as lateral boundary conditions produce a realistic evolution of the midtropospheric circulation. Vorticity errors of a 4-run simulation ensemble leveled off after about 3 days and thereafter hovered at values that were at least 30% lower than persistence errors.

The simulated distribution of daily precipitation has been validated over a 2-week period against rain gauge data and satellite infrared cloud imagery over West Africa. The correspondence between modeled precipitation distributions and observational evidence is best within the first 3 days after the initial conditions. Simulated precipitation rates became unrealistically lower after about 5 days and into the second week, perhaps related to a concomitant weaker circulation. Dramatic improvement in the time-space distribution of model precipitation for the last 9 days was accomplished by reinitializing the model with ECMWF data on day 5. It is not clear whether this reflects the range of model skill or the range of ECMWF analysis quality.

A prominent AWD traversed the entire span of West Africa during the first 5 days of the study and the RM simulated its circulation and an associated region of active moist convection that advanced westward ahead of the wave trough. The simulation showed that the AWD was most organized on day 3 when the zonal cellular structure was clearly discernable. The main area of associated precipitation was situated under the rising branch of the cells capped by a broad region of upper-tropospheric divergence and bracketed by descending branches about 15° to the east and west. ECMWF analyses, on the other hand, provided an imperfect picture of these divergence distributions owing to their coarse time-space resolution. Several of the other precipitation areas, both modeled and observed, were not associated with AWD-related uplift or lower-tropospheric confluence zones.

Wavelet analysis of the 700-mb meridional wind (v7) from the four simulations detected AWD with characteristic 3.9-day periodicity, although slightly longer periods dominated at 15°N, 0°–10°W. Periodic variability of v7 was stronger in the first week at 10°E and lasted

progressively longer in the downstream westward direction, spanning almost the entire 2-week length of the simulations at 10°W.

Two simulations forced by constant LBC showed considerable degradation of the circulation. Additional experiments implied that this negative impact of LBC could be related to the initialization procedure. Dynamic initialization may deprive the model of valuable information, which can be restored only when the LBC are updated with synchronous observational data. Moreover, in a single simulation without latent heat releases, constant LBC were also not quite as damaging to the model midtropospheric circulation, implying that the model may be more sensitive to constant LBC when there are strong feedbacks from high precipitation rates. Accordingly, initializing with a more compatible initial moisture field apparently increases the importance of latent heat feedbacks on the simulated circulation. These results may have implications for daily or seasonal predictions since such simulations cannot benefit from LBC derived from observations. However, since these inferences have been drawn from a limited number of simulations of a particular case study, they should be contemplated with caution. Finally, additional testing is needed to determine the sensitivity of model simulations to LBC supplied by GCMs, which do provide time-dependent information, although less realistic than data from updated observational analyses.

This study has demonstrated the utility of using high-resolution simulations for diagnostic investigations of African wave disturbances. Many more RM simulations need to be analyzed to generalize conclusions and to more completely document model performance. Still, these RM results are encouraging. These are necessary preliminaries to the application of regional models for weather and seasonal climate prediction over West Africa. Future work will accordingly evaluate monthly and seasonal mean fields forced by both analyses and GCMs.

Acknowledgments. This research was funded by the National Science Foundation under Grant ATM 97-25142, by the NASA Climate and Earth Observing System Programs, and by the National Research Council, National Academy of Sciences. Satellite images in Fig. 1 were created by Antoinette Wannebo based on data supplied by ISCCP.

REFERENCES

- Bounoua, L., 1992: Land surface processes and climate modeling. Ph.D. dissertation, The Florida State University, 196 pp.
- Burpee, R., 1972: The origin and structure of easterly waves in the lower troposphere of North Africa. *J. Atmos. Sci.*, **29**, 77–90.
- Dastoor, A., and T. N. Krishnamurti, 1991: Landfall and structure of a tropical cyclone: Sensitivity of the model predictions to soil moisture parameterization. *Bound.-Layer Meteor.*, **55**, 345–380.
- Deardoff, J., 1978: Efficient prediction of ground surface temperature and moisture with inclusion of a layer of vegetation. *J. Geophys. Res.*, **83**, 1889–1903.
- Diedhiou, A., S. Janicot, A. Viltard, P. de Felice, and H. Laurent, 1999: Easterly wave regimes and associated convection over West Africa and tropical Atlantic: Results from NCEP/NCAR and ECMWF reanalyses. *Climate Dyn.*, **15**, 795–822.
- Druyan, L., P. Lonergan, and M. Saloum, 1996: African wave disturbances and precipitation at Niamey during July–August 1987–1988. *Climate Res.*, **7**, 71–83.
- , —, and J. Cohen, 1997: Case studies of African wave disturbances in gridded analyses. *Mon. Wea. Rev.*, **125**, 2520–2530.
- , M. Fulakeza, and W. Thiaw, 2000: Regional model simulations of African wave disturbances. *J. Geophys. Res.*, **105**, 7231–7255.
- Fulakeza, M., 1998: Modeling regional climate of southern central Africa, Ph.D. dissertation, The Florida State University, 243 pp.
- Giorgi, F., and L. Mearns, 1999: Introduction to special section: Regional climate modeling revisited. *J. Geophys. Res.*, **104**, 6335–6352.
- Haltiner, G. J., and R. T. Williams, 1980: *Numerical Prediction and Dynamic Meteorology*. John Wiley and Sons, 477 pp.
- Jenkins, G., 1997: The 1988 and 1990 summer season simulations for West Africa using a regional climate model. *J. Climate*, **10**, 1255–1272.
- Kamara, S., 1986: The origins and types of rainfall in West Africa. *Weather*, **41**, 48–56.
- Krishnamurti, T. N., S. Low-Nam, and R. Pasch, 1983: Cumulus parameterization and rainfall rates II. *Mon. Wea. Rev.*, **111**, 815–828.
- , A. Kumar, K. S. Yap, A. P. Dastoor, N. Davidson, and J. Sheng, 1990: Performance of high resolution mesoscale tropical prediction model. *Advances in Geophysics*, Vol. 32, Academic Press, 133–286.
- Kumar, A., 1989: A documentation of the FSU limited area model. Report 89-4, Department of Meteorology, The Florida State University, 301 pp.
- Kuo, H., 1974: Further studies of the parameterization of the influence of cumulus convection on large-scale flow. *J. Atmos. Sci.*, **31**, 1232–1240.
- Peters, M., G. Tetzlaff, and W. Janssen, 1989: Rainfall intensity of West African squall lines. *Ann. Geophys.*, **7**, 227–238.
- Reed, R., D. Norquist, and E. Recker, 1977: The structure and properties of African wave disturbances as observed during phase III of GATE. *Mon. Wea. Rev.*, **105**, 317–333.
- , E. Klinker, and A. Holingsworth, 1988: The structure and characteristics of African easterly wave disturbances as determined from the ECMWF operational analysis/forecast system. *Meteor. Atmos. Phys.*, **38**, 22–33.
- Ross, R., 1991: Energies of African wave disturbances derived from the FSU global spectral model. *Meteor. Atmos. Phys.*, **45**, 135–158.
- Semazzi, F., N.-H. Lin, Y.-L. Lin, and F. Giorgi, 1993: A nested model study of the Sahelian climate response to SST anomalies. *Geophys. Res. Lett.*, **20**, 2897–2900.
- Sugi, M., 1986: Dynamic normal mode initialization. *J. Meteor. Soc. Japan*, **64**, 623–636.
- Sun, L., F. Semazzi, F. Giorgi, and L. Ogallo, 1999a: Application of the NCAR regional climate model to eastern Africa. 1. Simulation of the short rains of 1988. *J. Geophys. Res.*, **104**, 6529–6548.
- , —, —, and —, 1999b: Application of the NCAR regional climate model to eastern Africa. 2. Simulation of interannual variability of short rains. *J. Geophys. Res.*, **104**, 6549–6562.
- Torrence, C., and G. Compo, 1998: A practical guide to wavelet analysis. *Bull. Amer. Meteor. Soc.*, **79**, 61–78.
- Xue, Y., and J. Shukla, 1993: The influence of land surface properties on Sahel climate. Part I: Desertification. *J. Climate*, **6**, 2232–2245.